

# Zero-Gap Electrolyzers Accelerate Reconstruction of Cu<sub>2</sub>O-Derived Catalysts under CO<sub>2</sub> Reduction

Jehad Abed,<sup>▽</sup> Ivan Grigioni,<sup>▽</sup> Talha Kose, Wajdi Alnoush, Sungjin Park, Annalisa Polo, Byoung-Hoon Lee, David Sinton, Drew Higgins,\* and Edward H. Sargent\*



Cite This: *ACS Energy Lett.* 2024, 9, 6225–6232



Read Online

ACCESS |



Metrics & More

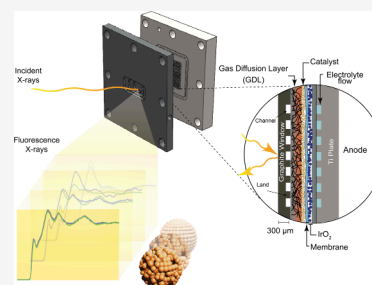


Article Recommendations



Supporting Information

**ABSTRACT:** To scale carbon dioxide reduction (CO<sub>2</sub>R), establishing a structure–property–performance relationship of the catalyst under the reaction conditions is a priority. Particularly in membrane electrode assembly (MEA) electrolyzers, knowledge about the valence state and coordination environment of the catalyst is of value yet limited. We developed an MEA electrolyzer that utilizes X-ray absorption spectroscopy to investigate the structural evolution of Cu<sub>2</sub>O-derived catalysts under CO<sub>2</sub>R and compare the same catalysts in a flow cell. Additionally, we study the influence of CO reduction and incorporating Ag on the reconstruction of the catalyst. We find that the strong reduction environment in the MEA and feeding CO leads to reconstruction of Cu<sub>2</sub>O particles, favoring higher coordination and lower oxidation states, which coincides with a shift in the reaction selectivity from C<sub>2+</sub> to hydrogen. Conversely, incorporating small amounts of Ag in the catalyst restricts the reconstruction. These findings advocate for *in situ* studies in zero-gap electrolyzers.



The design of carbon dioxide reduction (CO<sub>2</sub>R) electrochemical cells has been refined to enhance the energy efficiency and product selectivity. Initially, aqueous electrolyte cells with dissolved CO<sub>2</sub> were used;<sup>1–3</sup> however, the limited solubility of CO<sub>2</sub> in aqueous electrolytes (ca. 33 mM at standard conditions) restricts CO<sub>2</sub> availability at the electrode and limits the current density to ca. <20 mA cm<sup>-2</sup>.<sup>4,5</sup> Moreover, aqueous electrolytes provide an abundant source of protons, which can lead to the undesired hydrogen evolution reaction (HER).<sup>5</sup>

CO<sub>2</sub> flow electrolyzers, where separate streams of electrolyte flow past the cathode (catholyte) and anode (anolyte), offer improved mass transport of reactants to and products away from the electrode surfaces, thereby improving the reaction rate.<sup>6,7</sup> This makes them candidates for industrial scale applications of CO<sub>2</sub> electrolysis.<sup>6,7</sup> In particular, zero-gap membrane electrode assembly (MEA) electrolyzers feature a thin ion exchange membrane separating the cathode and anode, reducing ohmic losses and the full-cell voltage required to drive the electrochemical reaction compared to flow cells, which can experience larger ohmic losses due to electrolyte resistance within the larger fluid channels. However, electrolyzers, including MEA, alter the local reaction environment within the catalyst layer and, by extension, the properties of the catalyst, which significantly affects catalytic behavior.<sup>8–11</sup> Generally, the active state of the catalyst in electrocatalytic

cells, specially MEA, during CO<sub>2</sub>R remains to be fully investigated and continues to be a subject of debate.<sup>12–16</sup>

X-ray absorption spectroscopy (XAS) provides an opportunity to probe the local chemistry of catalysts *in situ* during the reaction, specially in aqueous flow electrolyzers.<sup>4</sup> However, deploying *in situ* XAS to study the catalyst in an MEA electrolyzer presents additional challenges.<sup>17</sup> In particular, the zero-gap configuration of the MEA electrolyzer requires that the cathode, membrane, and anode stack be compressed between two bipolar plates to reduce interfacial contact resistance and prevent electrolyte and gas leakages, which is not required in conventional aqueous flow cells. The bipolar plates must also contain flow fields to transport reactants (e.g., CO<sub>2</sub>, water) to the catalyst layer. These additional features of MEA pose challenges for *in situ* XAS because the compressed stack and bipolar plates can attenuate the X-ray beam, making it difficult to obtain clean and accurate measurements.

In this study, we devised an MEA electrolyzer that allows XAS probing of the catalyst without considerable attenuation

Received: September 23, 2024

Revised: October 29, 2024

Accepted: November 22, 2024

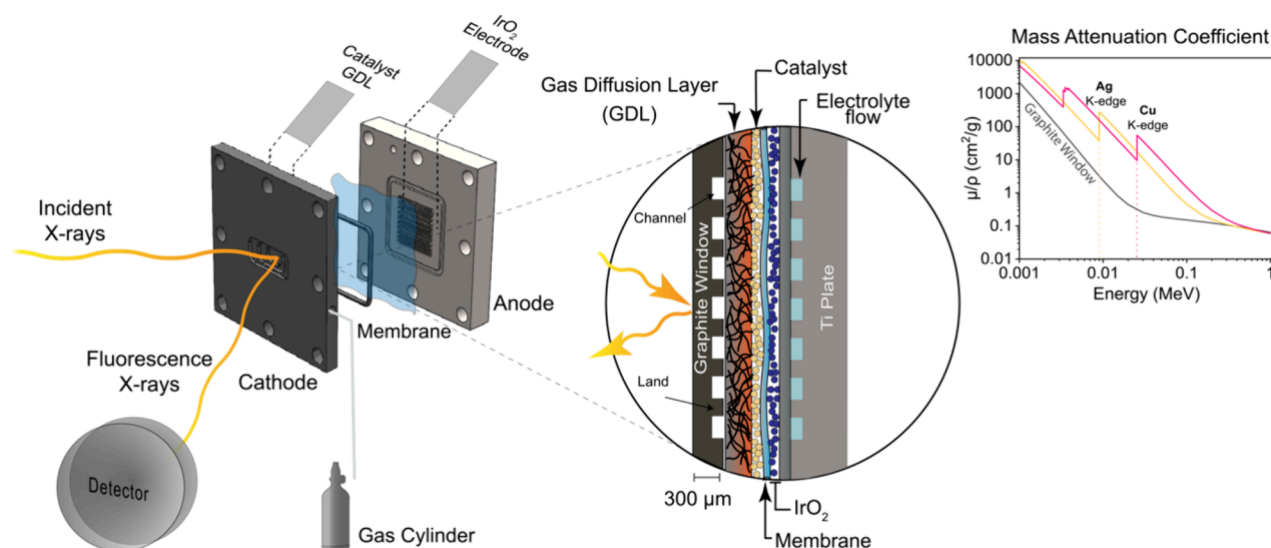


Figure 1. Cell design of membrane electrode assembly (MEA) electrolyzer for spectroscopy under reaction environments. Left: front view of the experimental setup with the orientation with respect to the X-ray beam and the detector for XAS measures. Center: magnified cross-sectional view of the membrane electrode assembly sandwiched between a graphite plate and titanium back plate. Right: mass attenuation ( $\mu/\rho$  is the mass attenuation coefficient, where  $\mu$  is the attenuation coefficient and  $\rho$  is the mass density) of graphite (window material), copper (yellow line), and silver (red line) as a function of incident X-ray energy. Notice that the stainless steel cathode back plate is not shown in this figure.

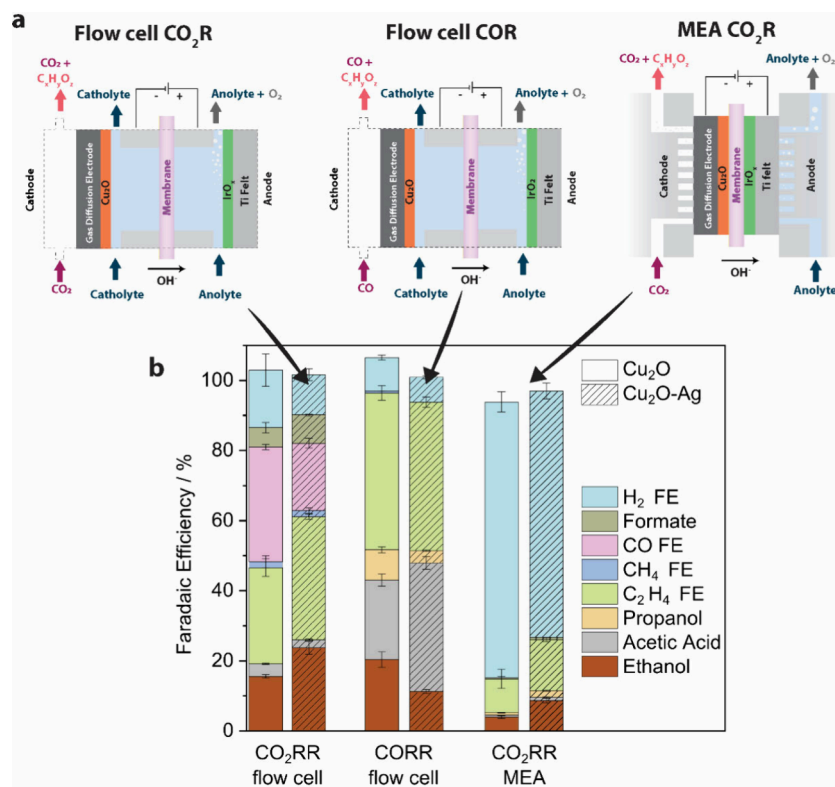
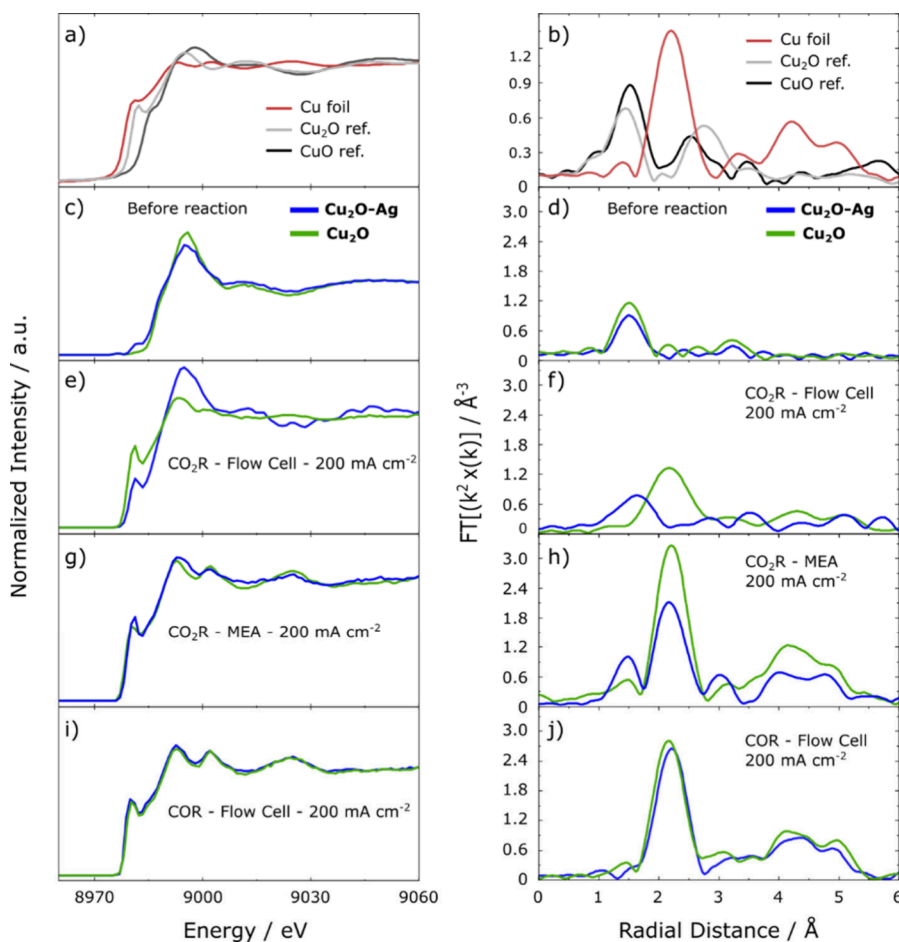


Figure 2. Electrochemical performance of Cu<sub>2</sub>O and Cu<sub>2</sub>O-Ag. (a) Three schematics showing the reaction configurations for CO<sub>2</sub> reduction in a flow cell (left) using 1 M KOH as catholyte, anolyte, and anion exchange membrane (AEM, Fumasep FAA-PK-130); CO reduction in a flow cell (middle) using 1 M KOH as catholyte, anolyte, and AEM (Fumasep FAA-PK-130); and CO<sub>2</sub> reduction in a membrane electrode assembly (MEA) cell (right) using 0.1 KHCO<sub>3</sub> as anolyte and AEM (Sustainion X37-50). (b) Product distribution as measured by gas chromatography for gas products and proton nuclear magnetic resonance for liquid products, showing the Faradaic efficiency (FE) of the reaction toward ethanol (CH<sub>3</sub>CH<sub>2</sub>OH), acetic acid (CH<sub>3</sub>COOH), propanol (CH<sub>3</sub>(CH<sub>2</sub>)<sub>2</sub>OH), ethylene (H<sub>2</sub>CCH<sub>2</sub>), methane (CH<sub>4</sub>), carbon monoxide (CO), formic acid (HCOOH), and hydrogen (H<sub>2</sub>). The solid bars represent experiments on Cu<sub>2</sub>O, while the hashed bars are for Cu<sub>2</sub>O-Ag.

in the signal. Using the designed cell, we investigated the structural stability of a Cu<sub>2</sub>O-derived catalyst *in situ* during

CO<sub>2</sub>R at 200 mA cm<sup>-2</sup>. We found that the cell architecture (MEA vs flow cell) strongly affected the structure and



**Figure 3.** Operando X-ray absorption results. The left panel shows the X-ray absorption near-edge structure (XANES), while the right panel shows the phase uncorrected radial distribution function (RDF) derived from extended X-ray absorption fine structures (EXAFS). (a, b) Measurements on standard samples of Cu foil, commercial Cu<sub>2</sub>O, and commercial CuO (not under reaction, in dry conditions). (c–j) Measurements on Cu<sub>2</sub>O (green curves) and Cu<sub>2</sub>O-Ag (blue curves) GDEs: (c, d) as-prepared samples (in dry conditions); operando measures under reaction conditions at 200 mA cm<sup>-2</sup> (e, f) in a flow cell, (g, h) in a membrane electrode assembly under CO<sub>2</sub>R, and (i, j) in a flow cell under COR. All spectra were collected and averaged over 20–30 min.

performance of the catalysts. Additionally, we studied the effect of reactant type (CO<sub>2</sub> vs CO) and the incorporation of Ag on the reconstruction behavior of the catalyst.

We designed our *in situ* XAS cell (Figure 1) by leveraging knowledge from previous advances in the fuel cell community.<sup>18–22</sup> A corrosion-resistant stainless steel front plate and a Ti back plate, electrochemically stable under harsh anodic oxidative conditions, form the conductive body of the cell and sandwich the MEA. The stainless steel front plate features a stepped edge X-ray window frame that allows a wide range of incident photon angles and reduces escape-cone losses of fluorescence X-rays (Figure 1a). The stainless steel plate supports a specially machined, conductive graphite plate, which is step engraved and milled as thin as 300 μm to enable X-ray penetration with a low mass attenuation coefficient ( $\mu/\rho$ ) at the K-edge energies of Cu and Ag. Additional details regarding the experimental setup of the cell and the preparation of the catalysts can be found in the Supporting Information (Figures S1 and S2).

We synthesized Cu<sub>2</sub>O via wet chemistry and Cu<sub>2</sub>O-Ag via galvanic exchange, as detailed in the Supporting Information and in our previous work.<sup>23</sup> During the synthesis of the Cu<sub>2</sub>O-Ag sample, Ag<sup>1+</sup> from the reaction solution displaces Cu<sup>1+</sup>, leading to surface Ag<sup>0</sup> (Figure S3) and Cu<sup>2+</sup> in solution. The

two nanopowders consist of porous, spherical 300 nm aggregates comprising smaller cuprite crystallites (Figures S4 and S5). The powders are mixed with Nafion in methanol and subsequently sprayed onto a gas diffusion electrode (GDE), as outlined in the Supporting Information. During sample preparation, the powder aggregates break apart, forming a continuous, porous network of 70–100 nm fragments (Figure S5).

We then tested Cu<sub>2</sub>O and Cu<sub>2</sub>O-Ag GDEs in three different reaction configurations (Figure 2a): CO<sub>2</sub>R in a flow cell, CO<sub>2</sub>R in an MEA, and CO reduction (COR) in a flow cell. In a CO<sub>2</sub>R flow cell configuration, both the Cu<sub>2</sub>O-Ag- and Cu<sub>2</sub>O-derived catalysts produced significant amounts of C<sub>2+</sub> products from CO<sub>2</sub>R at 200 mA cm<sup>-2</sup>. Galvanic replacement with Ag increased the Faradaic efficiency (FE) toward C<sub>2+</sub> by 14% (Figure 2b and Tables S1 and S2) and decreased FE toward CO by 13%. This is likely due to the role of Ag increasing the local concentration of adsorbed intermediate CO species (\*CO) on the catalyst surface<sup>24</sup> and promoting \*CO coupling, favoring C<sub>2+</sub> products.<sup>25</sup> However, when the catalysts were tested in the MEA electrolyzer, the selectivity for the CO<sub>2</sub>R products was substantially reduced compared to the flow cell configuration. The FE for H<sub>2</sub> increased from 21% to 83% for Cu<sub>2</sub>O and from 13% to 67% for Cu<sub>2</sub>O-Ag.<sup>26</sup>

**Table 1. Best-Fit Parameters Extracted from Cu K-Edge EXAFS for Cu<sub>2</sub>O<sup>a</sup>**

sample	fitting structure	shell	R (Å)	CN	$\sigma^2 \times 10^{-3}$ (Å)	$\Delta E$ (eV)
Cu <sub>2</sub> O/GDE dry	Cu <sub>2</sub> O	Cu–O1	1.95	2.04 ( $\pm 0.61$ )	1.19 ( $\pm 3.77$ )	4.53 ( $\pm 4.39$ )
flow Cu <sub>2</sub> O CO <sub>2</sub> R	Cu	Cu–Cu	2.53	6.03 ( $\pm 1.79$ )	10.72 ( $\pm 2.91$ )	1.68 ( $\pm 2.84$ )
MEA Cu <sub>2</sub> O CO <sub>2</sub> R	Cu	Cu–Cu	2.54	11.07 ( $\pm 1.74$ )	8.64 ( $\pm 1.41$ )	3.27 ( $\pm 1.50$ )
flow Cu <sub>2</sub> O COR	Cu	Cu–Cu	2.52	9.82 ( $\pm 3.15$ )	9.21 ( $\pm 2.94$ )	1.85 ( $\pm 3.12$ )

<sup>a</sup>R is the radical distance/bond length (with corrected phase shift). CN is the coordination number.  $\sigma^2$  is the Debye–Waller factor.  $\Delta E$  is the energy shift.

**Table 2. Best-Fit Parameters Extracted from Cu K-Edge EXAFS for Cu<sub>2</sub>O–Ag<sup>a</sup>**

sample	fitting structure	shell	R (Å)	CN	$\sigma^2 \times 10^{-3}$ (Å)	$\Delta E$ (eV)
Cu <sub>2</sub> O–Ag/GDE dry	Cu <sub>2</sub> O	Cu–O	1.93	1.88 ( $\pm 0.57$ )	2.77 ( $\pm 3.78$ )	2.80 ( $\pm 4.54$ )
flow Cu <sub>2</sub> O–Ag CO <sub>2</sub> R	Cu <sub>2</sub> O	Cu–O	1.97	1.53 ( $\pm 0.92$ )	3.62 ( $\pm 9.73$ )	9.85 ( $\pm 7.47$ )
MEA Cu <sub>2</sub> O–Ag CO <sub>2</sub> R	Cu <sub>2</sub> O	Cu–O	1.86	1.33 ( $\pm 0.56$ )	2.77 ( $\pm 3.78$ )	0.76 ( $\pm 3.47$ )
flow Cu <sub>2</sub> O–Ag COR	Cu	Cu–Cu	2.56	3.89 ( $\pm 1.33$ )	9.73 ( $\pm 3.33$ )	0.76 ( $\pm 3.47$ )
			2.56	10.14 ( $\pm 1.26$ )	9.74 ( $\pm 1.17$ )	3.18 ( $\pm 1.18$ )

<sup>a</sup>R is the radical distance/bond length (with corrected phase shift). CN is the coordination number.  $\sigma^2$  is the Debye–Waller factor.  $\Delta E$  is the energy shift.

Next, we probed the catalysts using *in situ* XAS to determine changes to the oxidation state and coordination environment of the catalysts under CO<sub>2</sub>R (Figure 3). We used commercial Cu foil, CuO, and Cu<sub>2</sub>O as reference materials for the calibration of the K-edge adsorption energies of Cu<sup>0</sup>, Cu<sup>1+</sup>, and Cu<sup>2+</sup> as shown by the X-ray absorption near-edge structure (XANES) analysis in Figure 3a. The Cu K-edge XANES spectrum showed a 0.58 eV shift toward lower energies for Cu<sub>2</sub>O–Ag compared to Cu<sub>2</sub>O (Figure 3c), suggesting that the overall oxidation state of Cu is slightly reduced upon Ag doping. To examine this closer, we used Fourier transform to generate a radial distribution function (RDF) from extended X-ray absorption fine structure (EXAFS) spectra (Figure 3, right panel). Both Cu<sub>2</sub>O and Cu<sub>2</sub>O–Ag (Figure 3d) showed a peak for Cu–O at approximately 1.5 Å, consistent with a +1 oxidation state, similar to the Cu<sub>2</sub>O standard (Figure 3b). Additionally, the coordination number (CN) of Cu–O was reduced from 2.04 in Cu<sub>2</sub>O to 1.88 in Cu<sub>2</sub>O–Ag, which could be a result of single-atom displacement of Cu with Ag (Tables 1 and 2).

To quantify the oxidation state distribution in the as-prepared catalysts, we performed linear combination fitting (LCF) on the XANES spectra (Figure 4). LCA fitting showed that the samples consisted primarily of more than 65 wt % Cu<sup>1+</sup>, while the rest was Cu<sup>2+</sup>. The presence of Cu<sup>2+</sup> is attributed to oxidation during sample preparation and storage in air.

Next, we incorporated the catalyst into a flow cell to study changes in the oxidation state and coordination environment during CO<sub>2</sub>R. It is crucial to highlight that the pumping of the catholyte over the catalyst in flow cells can cause mechanical vibrations and minor sample movements, leading to X-ray absorption perturbations, potentially diminishing the quality of EXAFS measurements. This may result in errors in the EXAFS fit with broader peaks potentially arising from measurement

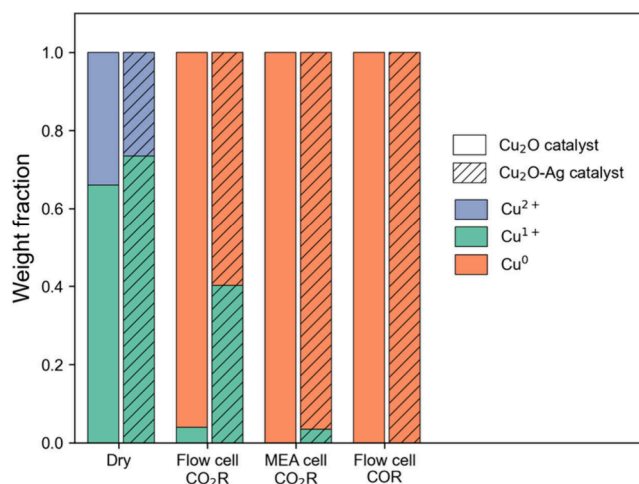


**Figure 4. Oxidation state evolution during the reaction. Calculated ratio of Cu oxidation states for as-prepared (dry) GDEs over the course of reduction at 200 mA cm<sup>-2</sup> under different reaction conditions, obtained by performing linear combination fitting of Cu K-edge X-ray absorption near-edge structure (XANES) spectra.**

noise. To mitigate this, we collected and averaged additional spectra for the flow cell configurations to reduce noise compared to the MEA experiments. When we ran the reaction at 200 mA cm<sup>-2</sup> (at -1.9 V vs the reversible hydrogen electrode, not *iR* corrected), we found that the pre-edge XANES intensity for both Cu<sub>2</sub>O and Cu<sub>2</sub>O–Ag was significantly increased, and the white line (peak centered at 8995 eV) was decreased, indicating the reduction of Cu. The LCF analysis showed that >92 wt % of the Cu species were reduced to Cu<sup>0</sup> for Cu<sub>2</sub>O, and <60 wt % were reduced in Cu<sub>2</sub>O–Ag. By examining the EXAFS results (Figure 3f), we noticed that the Cu–O peak at 1.5 Å in Cu<sub>2</sub>O disappeared while a new peak at 2.2 Å emerged, implying that Cu<sub>2</sub>O was



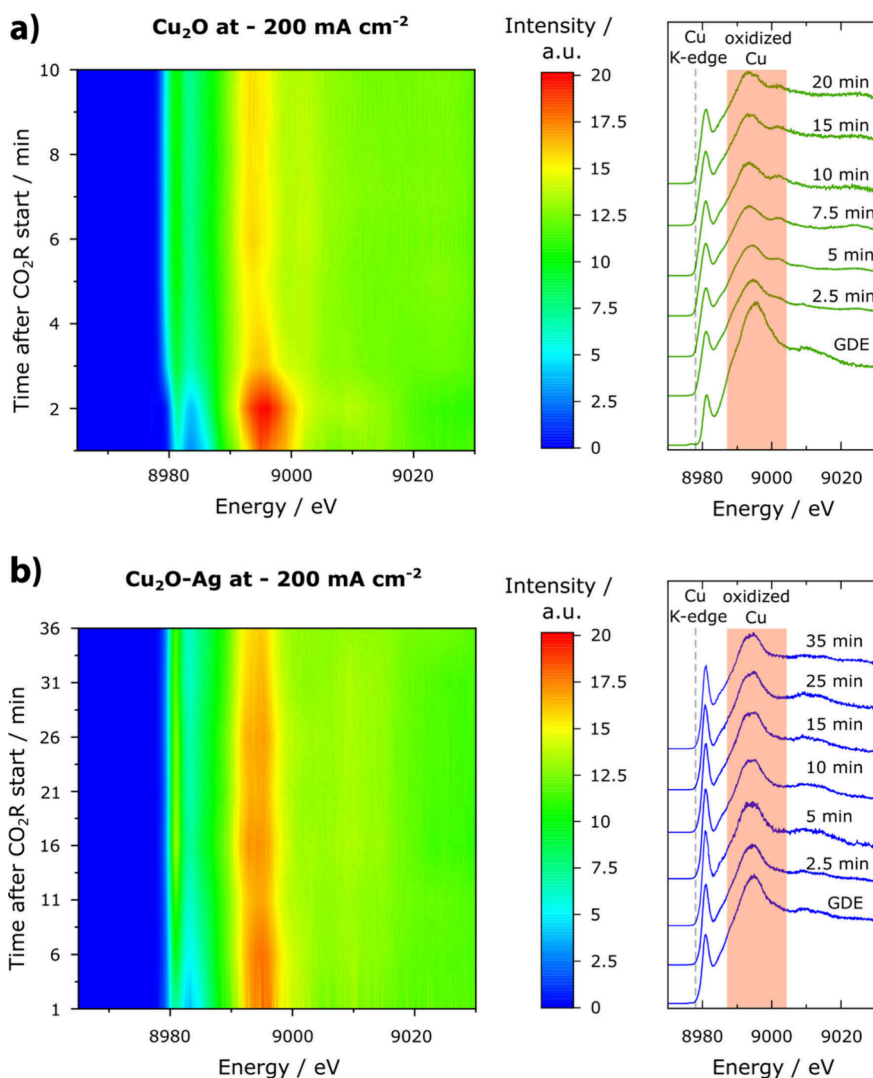


**Figure 5.** *Operando* time-resolved X-ray absorption results. The figures show (left) the contour plot of the X-ray fluorescence signal measured every 2 min of the CO<sub>2</sub> reduction at 200 mA cm<sup>-2</sup> and (right) the stack of X-ray absorption near-edge structure (XANES) spectra collected in a flow cell for (a) Cu<sub>2</sub>O and (b) Cu<sub>2</sub>O-Ag.

reduced to metallic Cu that is undercoordinated with CN = 6.03.

Despite the harsh reduction potential applied to the samples, Cu–O sites in Cu<sub>2</sub>O-Ag experienced little reconstruction (the coordination number remained close to 2 before and during the reaction) and preserved a more significant portion of their initial oxidation state compared to Cu<sub>2</sub>O (see Tables 1 and 2). To examine this more closely, we used time-resolved XANES to track the evolution of the oxidation state for Cu (Figure 5). We found that for the Cu<sub>2</sub>O-Ag sample, Cu remained partially oxidized for at least 40 min, while the white oxide peak for Cu<sub>2</sub>O faded within 2–4 min, reducing to metallic Cu as evident by the shift of the Cu K-edge toward 8979 eV.

The porous structure of both the Cu<sub>2</sub>O and Cu<sub>2</sub>O-Ag GDEs was still preserved after the reaction in the flow cell, as shown by the SEM images in Figures S5 and S6a,d. SAED analysis revealed that Cu<sub>2</sub>O experienced a more pronounced reduction than Cu<sub>2</sub>O-Ag, as indicated by the brighter metallic copper diffraction spots and the diminished diffraction ring signal for cuprite (Figure S6c,f), which agrees with the XAS analysis.

We then used the *in situ* MEA electrolyzer to observe the behavior of the catalysts in the MEA configuration (Figure

3g,h). The absence of the catholyte in this configuration minimizes the noise observed in the flow cell. The enhanced signal-to-noise ratio in MEA cells is a desirable feature, as it enables the acquisition of high-quality XAS data *in situ* for electrochemical reactions.

The XANES profiles for Cu<sub>2</sub>O and Cu<sub>2</sub>O-Ag in the flow and MEA electrolyzers looked similar at 200 mA cm<sup>-2</sup> (Figure 3g). However, EXAFS analysis (Figure 3h) revealed that both catalysts were reduced, as evident by the emergence of a metallic Cu–Cu peak at 2.2 Å and the extended structures after 4.5 Å, which could also be seen in the reference Cu foil (Figures 3b). This was also confirmed by the LCF analysis (Figure 4), where >90 wt % of Cu<sup>1+</sup> was reduced to Cu<sup>0</sup> for both Cu<sub>2</sub>O-Ag and Cu<sub>2</sub>O. The increase in peak intensity for the Cu–Cu bond at 2.2 Å indicates a change to the coordination environment due to substantial catalyst reconstruction in the MEA cell (Tables 1 and 2). The coordination number of Cu–Cu in the Cu<sub>2</sub>O sample was 11 during CO<sub>2</sub>R, which is close to that of the reference metallic Cu foil (CN = 12). SEM images show that running Cu<sub>2</sub>O-Ag GDE in the MEA electrolyzer created large Cu fragments (Figure S6g,h). These findings further corroborate that the catalysts undergo

significant structural transformations during CO<sub>2</sub>R in the MEA. It is worth noting that when we conducted time-resolved experiments with the MEA setup, we observed that the reduction kinetics were significantly faster compared to those in the flow cell. Given this rapid transition to metallic Cu, conducting time-resolved analysis would not provide useful insights with the current time resolution.

We switched the gas feed in the flow cell from CO<sub>2</sub> to CO to study the impact of CO on catalyst reconstruction (Figure 2b). This increased the FE to more than 90% for C<sub>2+</sub> products (ca. 40% increase compared to CO<sub>2</sub>R) for both Cu<sub>2</sub>O and Cu<sub>2</sub>O-Ag, due to the CO-rich reaction environment.<sup>27,28</sup> The two catalysts displayed high specific selectivity toward acetate (23% FE for Cu<sub>2</sub>O and 37% FE for Cu<sub>2</sub>O-Ag), implying significant changes to the reaction pathway when using CO as a reactant instead of CO<sub>2</sub>. We found, in our previous works, that this is ascribed to larger \*CO and carboxylate (\*COO<sup>-</sup>) intermediate adsorption favoring the acetate reaction pathway and catholyte alkalinity, which provides improved energetics for C<sub>2+</sub> formation.<sup>23,29</sup>

*In situ* XAS under COR showed that both catalysts Cu<sub>2</sub>O and Cu<sub>2</sub>O-Ag were largely reduced, as indicated by the well-defined pre-edge peak and the rise of an intense Cu–Cu peak at 2.2 Å (Figures 3i,j). Moreover, the coordination numbers for Cu<sub>2</sub>O (CN = 9.82) and Cu<sub>2</sub>O-Ag (CN = 10.14) during COR were much higher than those for CO<sub>2</sub>R in the flow cell under similar reaction conditions (Tables 1 and 2), suggesting that the catalysts had undergone stronger reduction in COR than CO<sub>2</sub>R. This could be ascribed to the high local concentration of CO on the catalyst surface in COR, which can adversely affect the structural stability of Cu. We also propose that any Cu–O sites that were electronically isolated within the Cu<sub>2</sub>O-Ag electrode could have been reduced due to the inherent reducing capabilities of CO.<sup>14</sup>

Our observations from the XAS studies shed light on the behavior of Cu<sub>2</sub>O-derived catalysts during CO<sub>2</sub>R and COR. It revealed that the choice of cell configuration (aqueous flow electrolyte vs solid polymer membrane cells) and reactant type (CO<sub>2</sub> vs CO) significantly influenced the stability of Cu<sup>1+</sup> species during the reaction.

We attribute the observed differences in the oxidation state of Cu between the different reactor configurations to the distinct reaction environments in the MEA electrolyzer and flow cells. The serpentine flow field design of the MEA electrolyzer helps facilitate a uniform interaction between the reactants and the electrode. This promotes an evenly distributed current density across the catalyst, reducing more Cu<sup>1+</sup> sites to Cu<sup>0</sup>. Conversely, catalysts in flow cells can exhibit nonuniform current distributions due to variations in reactant concentration or poor electronic conductivity across the catalyst layer. This results in inconsistent reconstruction behavior of Cu at different catalyst locations. Iglesias van Montfort et al. employed IR thermography to investigate the electrocatalytic activity of GDE in flow cell electrolyzers, noting significant temperature variations across the catalyst during CO<sub>2</sub>R.<sup>30</sup> These variations stem from spatial differences in localized current density and can lead to uneven catalyst reconstruction.

During the CO<sub>2</sub>R reaction in a flow cell, we noted that Cu did not fully reduce but remained partially oxidized for both Cu<sub>2</sub>O and Cu<sub>2</sub>O-Ag. Interestingly, incorporating small amounts of Ag in Cu<sub>2</sub>O restricted the reconstruction of the catalyst during the reaction. Spatial confinement of reaction

intermediates on the catalyst's surface<sup>31</sup> and the presence of dispersed Ag atoms in the Cu<sub>2</sub>O-Ag surface could have prevented the further reduction of Cu<sup>1+</sup> species and the reconstruction of the surface, trapping metastable Cu–O–Ag sites.<sup>32,33</sup> Additionally, we conjecture that the CO<sub>2</sub>R predominantly occurred at metallic (reduced) Cu atoms adjacent to Ag atoms (Cu–Ag) on the surface. Meanwhile, a portion of Cu-based atoms (or particles) stayed oxidized and electronically isolated, rendering them electrocatalytically inactive.<sup>34</sup>

Moreover, we found that Cu<sub>2</sub>O in both the MEA electrolyzer during CO<sub>2</sub>R and the flow cell during COR was reduced to metallic Cu, which significantly increased the coordination number. Although Cu in both scenarios had a similar valence state and coordination number, the selectivities of these two reactions were significantly different. COR predominantly produced C<sub>2+</sub> products with high FE, whereas CO<sub>2</sub>R in the MEA primarily led to HER. The notable shift in FE indicates a substantial change in the accessibility of reactants to the active sites (mass transport) in the MEA configuration compared to the flow cell, contributing to the pronounced differences in HER selectivity. However, factors such as increased ionic conductivity or local hydroxide concentration in the MEA can lead to a higher salt concentration near the catalyst surface, affecting the reaction microenvironment. This, in turn, can cause local pH variations, which significantly influence the selectivity of the reaction.<sup>35–38</sup> There is also the possibility that CO<sub>2</sub>R and COR occurred at different active sites along the catalytic pathway to the products. This has been experimentally confirmed by Gao et al. using labeling experiments with mixed CO<sub>2</sub>/CO gas feeds and *operando* Raman spectroscopy.<sup>39</sup> They showed that CO adsorbed on defective Cu sites is at least six times more active toward C<sub>2+</sub> than CO<sub>2</sub> on Cu sites. Nonetheless, a detailed investigation of these additional factors extends beyond the scope of this current study and has been addressed in other research works.<sup>35–39</sup>

These findings highlight the importance of utilizing *in situ* zero-gap electrolyzers to gain insight into the reconstruction mechanisms of catalysts under industrial operating conditions.

## ■ ASSOCIATED CONTENT

### SI Supporting Information

The Supporting Information is available free of charge at <https://pubs.acs.org/doi/10.1021/acsenergylett.4c02634>.

Experimental details, XANES spectra, EXAFS results, TEM and SEM images, and FE data (PDF)

## ■ AUTHOR INFORMATION

### Corresponding Authors

Edward H. Sargent – Department of Electrical and Computer Engineering, University of Toronto, Toronto, Ontario M5S 1A4, Canada; The Alliance for AI-Accelerated Materials Discovery (A3MD), <https://a3md.utoronto.ca>; [orcid.org/0000-0003-0396-6495](https://orcid.org/0000-0003-0396-6495); Email: [ted.sargent@utoronto.ca](mailto:ted.sargent@utoronto.ca)

Drew Higgins – Department of Chemical Engineering, McMaster University, Hamilton, Ontario L8S 4L7, Canada; [orcid.org/0000-0002-0585-2670](https://orcid.org/0000-0002-0585-2670); Email: [higgid2@mcmaster.ca](mailto:higgid2@mcmaster.ca)

## Authors

Jehad Abed – Department of Materials Science and Engineering, University of Toronto, Toronto, Ontario M5S 3E4, Canada; Department of Electrical and Computer Engineering, University of Toronto, Toronto, Ontario M5S 1A4, Canada; The Alliance for AI-Accelerated Materials Discovery (A3MD), <https://a3md.utoronto.ca>;  
orcid.org/0000-0003-1387-2740

Ivan Grigioni – Department of Electrical and Computer Engineering, University of Toronto, Toronto, Ontario M5S 1A4, Canada; Department of Chemistry, University of Milan, 20133 Milano, MI, Italy; orcid.org/0000-0002-9469-4570

Talha Kose – Department of Mechanical and Industrial Engineering, University of Toronto, Toronto, Ontario M5S 3G8, Canada; The Alliance for AI-Accelerated Materials Discovery (A3MD), <https://a3md.utoronto.ca>

Wajdi Alnough – Department of Chemical Engineering, McMaster University, Hamilton, Ontario L8S 4L7, Canada; The Alliance for AI-Accelerated Materials Discovery (A3MD), <https://a3md.utoronto.ca>

Sungjin Park – Department of Electrical and Computer Engineering, University of Toronto, Toronto, Ontario M5S 1A4, Canada

Annalisa Polo – Department of Chemistry, University of Milan, 20133 Milano, MI, Italy; orcid.org/0000-0001-5724-2607

Byoung-Hoon Lee – Department of Electrical and Computer Engineering, University of Toronto, Toronto, Ontario M5S 1A4, Canada; Graduate School of Converging Science and Technology, Korea University, Seoul 02481, Republic of Korea

David Sinton – Department of Mechanical and Industrial Engineering, University of Toronto, Toronto, Ontario M5S 3G8, Canada; The Alliance for AI-Accelerated Materials Discovery (A3MD), <https://a3md.utoronto.ca>

Complete contact information is available at:

<https://pubs.acs.org/10.1021/acseenergylett.4c02634>

## Author Contributions

<sup>†</sup>J.A. and I.G. contributed equally to this work.

## Notes

The authors declare no competing financial interest.

## ACKNOWLEDGMENTS

We acknowledge the European Synchrotron Radiation Facility (ESRF) for provision of synchrotron radiation facilities, and we would like to thank Dr. Viktoriia Saveleva and Dr. Pieter Glatzel for the assistance and support in using beamline ID26 during the experimental session MA5352 (10.1515/ESRF-ES-744180074). J.A. acknowledges the Natural Sciences and Engineering Research Council (NSERC) of Canada under a Vanier Canada Graduate Scholarship (Grant 705992). I.G. acknowledges the European Union's Horizon 2020 research and innovation programme under a Marie Skłodowska-Curie grant (Agreement 846107) and the Università degli Studi di Milano for grant CLHC (PSR\_Line4). The authors also acknowledge support from the Alliance for AI-Accelerated Materials discovery (A3MD).

## REFERENCES

- (1) Murata, A.; Hori, Y. Product Selectivity Affected by Cationic Species in Electrochemical Reduction of CO<sub>2</sub> and CO at a Cu Electrode. *Bull. Chem. Soc. Jpn.* **1991**, *64* (1), 123–127.
- (2) Kuhl, K. P.; Cave, E. R.; Abram, D. N.; Jaramillo, T. F. New Insights into the Electrochemical Reduction of Carbon Dioxide on Metallic Copper Surfaces. *Energy Environ. Sci.* **2012**, *5* (5), 7050–7059.
- (3) Whipple, D. T.; Kenis, P. J. A. Prospects of CO<sub>2</sub> Utilization via Direct Heterogeneous Electrochemical Reduction. *J. Phys. Chem. Lett.* **2010**, *1* (24), 3451–3458.
- (4) Clark, E. L.; Resasco, J.; Landers, A.; Lin, J.; Chung, L. T.; Walton, A.; Hahn, C.; Jaramillo, T. F.; Bell, A. T. Standards and Protocols for Data Acquisition and Reporting for Studies of the Electrochemical Reduction of Carbon Dioxide. *ACS Catal.* **2018**, *8* (7), 6560–6570.
- (5) Higgins, D.; Hahn, C.; Xiang, C.; Jaramillo, T. F.; Weber, A. Z. Gas-Diffusion Electrodes for Carbon Dioxide Reduction: A New Paradigm. *ACS Energy Lett.* **2019**, *4* (1), 317–324.
- (6) Gabardo, C. M.; O'Brien, C. P.; Edwards, J. P.; McCallum, C.; Xu, Y.; Dinh, C. T.; Li, J.; Sargent, E. H.; Sinton, D. Continuous Carbon Dioxide Electroreduction to Concentrated Multi-Carbon Products Using a Membrane Electrode Assembly. *Joule* **2019**, *3* (11), 2777–2791.
- (7) Dinh, C.-T.; Burdyny, T.; Kibria, G.; Seifitokaldani, A.; Gabardo, C. M.; Garcia De Arquer, F. P.; Kiani, A.; Edwards, J. P.; De Luna, P.; Bushuyev, O. S.; Zou, C.; Quintero-Bermudez, R.; Pang, Y.; Sinton, D.; Sargent, E. H. CO<sub>2</sub> Electroreduction to Ethylene via Hydroxide-Mediated Copper Catalysis at an Abrupt Interface. *Science* **2018**, *360* (6390), 783–787.
- (8) Xu, Q.; Garg, S.; Moss, A. B.; Mirolo, M.; Chorkendorff, I.; Drnc, J.; Seger, B. Identifying and Alleviating the Durability Challenges in Membrane-Electrode-Assembly Devices for High-Rate CO Electrolysis. *Nat. Catal.* **2023**, *6*, 1042–1051.
- (9) Vennekoetter, J. B.; Sengpiel, R.; Wessling, M. Beyond the Catalyst: How Electrode and Reactor Design Determine the Product Spectrum during Electrochemical CO<sub>2</sub> Reduction. *Chemical Engineering Journal* **2019**, *364*, 89–101.
- (10) Kim, J. Y.; Sellers, C.; Hao, S.; Senftle, T. P.; Wang, H. Different Distributions of Multi-Carbon Products in CO<sub>2</sub> and CO Electroreduction under Practical Reaction Conditions. *Nature Catalysis* **2023**, *6* (12), 1115–1124.
- (11) Choi, W.; Chae, Y.; Liu, E.; Kim, D.; Drisdell, W. S.; Oh, H. S.; Koh, J. H.; Lee, D. K.; Lee, U.; Won, D. H. Exploring the Influence of Cell Configurations on Cu Catalyst Reconstruction during CO<sub>2</sub> Electroreduction. *Nature Communications* **2024**, *15* (1), 1–11.
- (12) Wang, X.; Klingan, K.; Klingenhof, M.; Möller, T.; Ferreira de Araújo, J.; Martens, I.; Bagger, A.; Jiang, S.; Rossmeis, J.; Dau, H.; Strasser, P. Morphology and Mechanism of Highly Selective Cu(II) Oxide Nanosheet Catalysts for Carbon Dioxide Electroreduction. *Nature Communications* **2021**, *12* (1), 1–12.
- (13) Vavra, J.; Shen, T. H.; Stoian, D.; Tileli, V.; Buonsanti, R. Real-Time Monitoring Reveals Dissolution/Redeposition Mechanism in Copper Nanocatalysts during the Initial Stages of the CO<sub>2</sub> Reduction Reaction. *Angew. Chem., Int. Ed.* **2021**, *60* (3), 1347–1354.
- (14) Wilde, P.; O'Mara, P. B.; Junqueira, J. R. C.; Tarnev, T.; Benedetti, T. M.; Andronescu, C.; Chen, Y. T.; Tilley, R. D.; Schuhmann, W.; Gooding, J. J. Is Cu Instability during the CO<sub>2</sub> Reduction Reaction Governed by the Applied Potential or the Local CO Concentration? *Chem. Sci.* **2021**, *12* (11), 4028–4033.
- (15) Hung, S. F.; Wu, F. Y.; Lu, Y. H.; Lee, T. J.; Tsai, H. J.; Chen, P. H.; Lin, Z. Y.; Chen, G. L.; Huang, W. Y.; Zeng, W. J. Operando X-Ray Absorption Spectroscopic Studies of the Carbon Dioxide Reduction Reaction in a Modified Flow Cell. *Catal. Sci. Technol.* **2022**, *12* (9), 2739–2743.
- (16) Yang, Y.; Louisia, S.; Yu, S.; Jin, J.; Roh, I.; Chen, C.; Fonseca Guzman, M. V.; Feijóo, J.; Chen, P. C.; Wang, H.; Pollock, C. J.; Huang, X.; Shao, Y. T.; Wang, C.; Muller, D. A.; Abruña, H. D.; Yang,



- P. Operando Studies Reveal Active Cu Nanograins for CO<sub>2</sub> Electroreduction. *Nature* 2023 614:7947 **2023**, 614 (7947), 262–269.
- (17) Moss, A. B.; Häätinen, J.; Kúš, P.; Garg, S.; Mirolo, M.; Chorkendorff, I.; Seger, B.; Drnec, J. Versatile High Energy X-Ray Transparent Electrolysis Cell for Operando Measurements. *J. Power Sources* **2023**, 562, 232754.
- (18) Lewis, E. A.; Kendrick, I.; Jia, Q.; Grice, C.; Segre, C. U.; Smotkin, E. S. Operando X-Ray Absorption and Infrared Fuel Cell Spectroscopy. *Electrochim. Acta* **2011**, 56, 8827–8832.
- (19) Gilbert, J. A.; Kariuki, N. N.; Wang, X.; Kropf, A. J.; Yu, K.; Groom, D. J.; Ferreira, P. J.; Morgan, D.; Myers, D. J. Pt Catalyst Degradation in Aqueous and Fuel Cell Environments Studied via In-Operando Anomalous Small-Angle X-Ray Scattering. *Electrochim. Acta* **2015**, 173, 223–234.
- (20) Leach, A. S.; Hack, J.; Amboage, M.; Diaz-Moreno, S.; Huang, H.; Cullen, P. L.; Wilding, M.; Magliocca, E.; Miller, T. S.; Howard, C. A.; Brett, D. J. L.; Shearing, P. R.; McMillan, P. F.; Russell, A. E.; Jarvis, R. A Novel Fuel Cell Design for Operando Energy-Dispersive x-Ray Absorption Measurements. *J. Phys.: Condens. Matter* **2021**, 33 (31), 314002.
- (21) Viswanathan, R.; Liu, R.; Smotkin, E. S. In Situ X-Ray Absorption Fuel Cell. *Rev. Sci. Instrum.* **2002**, 73 (5), 2124–2127.
- (22) Nakanishi, K.; Kato, D.; Arai, H.; Tanida, H.; Mori, T.; Orikasa, Y.; Uchimoto, Y.; Ohta, T.; Ogumi, Z. Novel Spectro-Electrochemical Cell for in Situ/Operando Observation of Common Composite Electrode with Liquid Electrolyte by X-Ray Absorption Spectroscopy in the Tender X-Ray Region. *Rev. Sci. Instrum.* **2014**, 85 (8), 084103.
- (23) Dorakhan, R.; Grigioni, I.; Lee, B.-H.; Ou, P.; Abed, J.; O'Brien, C.; Sedighian Rasouli, A.; Plodinec, M.; Miao, R. K.; Shirzadi, E.; Wicks, J.; Park, S.; Lee, G.; Zhang, J.; Sinton, D.; Sargent, E. H. A Silver-Copper Oxide Catalyst for Acetate Electrosynthesis from Carbon Monoxide. *Nature Synthesis* 2023 2:5 **2023**, 2 (5), 448–457.
- (24) Higgins, D.; Landers, A. T.; Ji, Y.; Nitopi, S.; Morales-Guio, C. G.; Wang, L.; Chan, K.; Hahn, C.; Jaramillo, T. F. Guiding Electrochemical Carbon Dioxide Reduction toward Carbonyls Using Copper Silver Thin Films with Interphase Miscibility. *ACS Energy Lett.* **2018**, 3 (12), 2947–2955.
- (25) Li, Y. C.; Wang, Z.; Yuan, T.; Nam, D.-H.; Luo, M.; Wicks, J.; Chen, B.; Li, J.; Li, F.; De Arquer, F. P. G.; Wang, Y.; Dinh, C.-T.; Voznyy, O.; Sinton, D.; Sargent, E. H. Binding Site Diversity Promotes CO<sub>2</sub> Electroreduction to Ethanol. *J. Am. Chem. Soc.* **2019**, 141 (21), 8584–8591.
- (26) Hoang, T. T. H.; Verma, S.; Ma, S.; Fister, T. T.; Timoshenko, J.; Frenkel, A. I.; Kenis, P. J. A.; Gewirth, A. A. Nanoporous Copper-Silver Alloys by Additive-Controlled Electrodeposition for the Selective Electroreduction of CO<sub>2</sub> to Ethylene and Ethanol. *J. Am. Chem. Soc.* **2018**, 140 (17), 5791–5797.
- (27) Verdaguier-Casadevall, A.; Li, C. W.; Johansson, T. P.; Scott, S. B.; McKeown, J. T.; Kumar, M.; Stephens, I. E. L.; Kanan, M. W.; Chorkendorff, I. Probing the Active Surface Sites for CO Reduction on Oxide-Derived Copper Electrocatalysts. *J. Am. Chem. Soc.* **2015**, 137 (31), 9808–9811.
- (28) Li, C. W.; Ciston, J.; Kanan, M. W. Electroreduction of Carbon Monoxide to Liquid Fuel on Oxide-Derived Nanocrystalline Copper. *Nature* **2014**, 508 (7497), 504–507.
- (29) Wang, L.; Nitopi, S. A.; Bertheussen, E.; Orazov, M.; Morales-Guio, C. G.; Liu, X.; Higgins, D. C.; Chan, K.; Nørskov, J. K.; Hahn, C.; Jaramillo, T. F. Electrochemical Carbon Monoxide Reduction on Polycrystalline Copper: Effects of Potential, Pressure, and PH on Selectivity toward Multicarbon and Oxygenated Products. *ACS Catal.* **2018**, 8 (8), 7445–7454.
- (30) Iglesias van Montfort, H. P.; Burdyny, T. Mapping Spatial and Temporal Electrochemical Activity of Water and CO<sub>2</sub> Electrolysis on Gas-Diffusion Electrodes Using Infrared Thermography. *ACS Energy Lett.* **2022**, 7 (8), 2410–2419.
- (31) Yang, P.-P.; Zhang, X.-L.; Gao, F.-Y.; Zheng, Y.-R.; Niu, Z.-Z.; Yu, X.; Liu, R.; Wu, Z.-Z.; Qin, S.; Chi, L.-P.; Duan, Y.; Ma, T.; Zheng, X.-S.; Zhu, J.-F.; Wang, H.-J.; Gao, M.-R.; Yu, S.-H. Protecting Copper Oxidation State via Intermediate Confinement for Selective CO<sub>2</sub> Electroreduction to C<sub>2</sub>+ Fuels. *J. Am. Chem. Soc.* **2020**, 142 (13), 6400–6408.
- (32) Tan, X.; Sun, K.; Zhuang, Z.; Hu, B.; Zhang, Y.; Liu, Q.; He, C.; Xu, Z.; Chen, C.; Xiao, H.; Chen, C. Stabilizing Copper by a Reconstruction-Resistant Atomic Cu-O-Si Interface for Electrochemical CO<sub>2</sub> Reduction. *J. Am. Chem. Soc.* **2023**, 145, 8656.
- (33) Jeong, H.; Shin, D.; Kim, B. S.; Bae, J.; Shin, S.; Choe, C.; Han, J. W.; Lee, H. Controlling the Oxidation State of Pt Single Atoms for Maximizing Catalytic Activity. *Angewandte Chemie - International Edition* **2020**, 59 (46), 20691–20696.
- (34) Zhang, C.; Eraky, H.; Tan, S.; Hitchcock, A.; Higgins, D. In Situ Studies of Copper-Based CO<sub>2</sub> Reduction Electrocatalysts by Scanning Transmission Soft X-Ray Microscopy. *ACS Nano* **2023**, 17 (21), 21337–21348.
- (35) Pan, B.; Wang, Y.; Li, Y. Understanding and Leveraging the Effect of Cations in the Electrical Double Layer for Electrochemical CO<sub>2</sub> Reduction. *Chem. Catalysis* **2022**, 2 (6), 1267–1276.
- (36) Marcandalli, G.; Monteiro, M. C. O.; Goyal, A.; Koper, M. T. M. Electrolyte Effects on CO<sub>2</sub> Electrochemical Reduction to CO. *Acc. Chem. Res.* **2022**, 55 (14), 1900–1911.
- (37) Disch, J.; Bohn, L.; Metzler, L.; Vierrath, S. Strategies for the mitigation of salt precipitation in zero-gap CO<sub>2</sub> electrolyzers producing CO. *J. Mater. Chem. A* **2023**, 11, 7344.
- (38) Sassenburg, M.; Kelly, M.; Subramanian, S.; Smith, W. A.; Burdyny, T. Zero-Gap Electrochemical CO<sub>2</sub> Reduction Cells: Challenges and Operational Strategies for Prevention of Salt Precipitation. *Cite This: ACS Energy Lett.* **2023**, 8, 321–331.
- (39) Gao, W.; Xu, Y.; Fu, L.; Chang, X.; Xu, B. Experimental Evidence of Distinct Sites for CO<sub>2</sub>-to-CO and CO Conversion on Cu in the Electrochemical CO<sub>2</sub> Reduction Reaction. *Nature Catalysis* 2023 6:10 **2023**, 6 (10), 885–894.